The correction of the energy response for the imaging detector based on the monolithic crystal

Haoxuan Li [1], Lei Wang [1,*], Yukun Du [1], Menglei Chen [1], Wei Lu [2], Zexi Wang [1]

[1]Chengdu University of Technology, Sichuan, Chengdu, 610059, China

[2]The Engineering & Technical College of Chengdu University of Technology, Sichuan, Leshan, 614000, China

*Corresponding author. *E-mail address:* wl@cdut.edu.cn

Abstract: The energy response of an imaging detector based on a monolithic crystal is highly dependent on the position of the gamma ray interaction, which leads to a spectral drift of the imaging detector, known as the spectral drift related to incident position. It deteriorates the energy resolution of the detector and affects the selection of the energy window for imaging, resulting in artefacts in the reconstructed image. Thus, an energy response correction method is proposed to improve the positional consistency of the detector energy response. In both simulation and physical experiments, the method improved the full-energy peak consistency of the monolithic crystal detector, which results in improved energy resolution of the detector, more accurate selection of the energy window, and imaging quality. Especially, in physical experiments, the method converges the peak sites of 365keV energy at each location, which reduced the half-height width of characteristic peak (@365 keV) from 53 to 38 channels, improved the energy resolution by 28.3%, transformed the incomplete mask projection into a complete mask projection, and the signal-to-noise ratio increased from 2.38 to 5.37.

Key words: monolithic crystal detector; SiPM array; spectral drift; energy response correction method

1.Introduction

In recent years, with the development of inorganic scintillators and optoelectronic sensors, scintillator detectors have been widely used in the fields of nuclear physics, particle physics and radiation imaging [1-12]. Scintillator crystals have the advantages of high optical yield, short decay time, high energy resolution, etc, which make them ideal crystal materials for the development of nuclear instruments [13]. Two types of scintillator crystals are mainly used in γ-radiation imaging: array crystals and monolithic crystals [14,15]. Imaging detectors with array crystals are less affected by compression effects and can achieve higher spatial resolution, which is mainly determined by the pixel size of the crystal array. The disadvantages of this detector are the absorption of photons between the crystal pixels by the reflective layer material and the thickness of the crystal arrays which significantly reduces its energy resolution and detection efficiency. In the imaging detector composed of array crystal coupled photomultiplier tube or silicon photomultiplier tube, the spectral peaks of

each crystal strip differ greatly [16,17].

Compared with array detectors, monolithic crystals have better energy resolution and detection efficiency. The disadvantage of the detector is that it is seriously affected by the compression effect, and the Useful Field-of-View (UFOV) is much smaller than the effective detector area of the detector. In recent years, many researchers mainly used the Truncated Centre-of-Gravity (TCOG), the Raise-to-Power (RTP; also known as Floating Weight, FW), the Least Squares Estimator, LSE), the Maximum Likelihood (ML), Artificial Neural Network (ANN), and other algorithms improve the compression effect of monolithic crystal imaging detectors and increase the UFOV [18-23]. In monolithic crystal imaging detectors, the energy response is highly dependent on the location of the gamma-ray interaction. When gamma rays interact at the edge of the crystal, the fluorescence distribution is truncated. And the photons in the crystal are affected by their structure and physical properties, changing their propagation direction and causing a loss of light. It results in inconsistent energy responses in monolithic crystal imaging detectors. It also causes the phenomenon of the inconsistency of the full-energy peak, that is, the spectral drift related to incident position. This results in a decrease in energy resolution, which affects nuclide recognition. For systems with a fixed region of interest (ROI), it leads to a decrease in the number of particles in the ROI, which affects the measurement accuracy and increases the measurement error. In the practical application of coded aperture gamma imaging system, the energy window will be selected. If the peak consistency correction is not carried out, the detector energy resolution will be decreased, which will lead to the loss of real cases, that is, the detection efficiency will be decreased, and then affect the imaging effect. Therefore, based on the previous simulation experiments of our research group [24], this paper verified the phenomenon through physical experiments, and adopted the energy response functional correction matrix. to enhance the peak position consistency, improve the energy resolution and the imaging quality.

2.Simulation and physical experiment

An imaging detector model was established using Geant4, and a step-scanning method was employed to acquire the spectral drift related to incident position. Additionally, we have established a radiation imaging system based on the model, and the electronic system and data processing system were introduced. Following the methods of simulation experiments, we have confirmed the spectral drift related to incident position also exists in physical experiments, which is even more severe in physical experiments.

2.1 Simulation experiment

In order to investigate the spectral drift related to incident position, we construct a model of an imaging detector based on monolithic scintillator using GEANT4 software, as shown in Figure 1c. The crystal employed in the model is a monolithic $LaBr_3(Ce)$ crystal, known for its exceptional properties including density, energy resolution, light yield, and decay time. The specific properties of the $LaBr_3(Ce)$

crystal are provided in Table 1. Figure 1 illustrates the structure of the detector and the process of step scanning. The detector is modelled with a $51mm \times 51mm \times 5mm$ LaBr$_3$(Ce) crystal. The LaBr$_3$(Ce) crystal was coated with a Teflon foil (0.3mm thickness) which acts as the front diffuse reflective layer. The scintillator was surrounded and encapsulated by an aluminum foil (0.5mm thickness) for the specular reflective layer [25]. A glass layer (3mm thickness, reflectivity 1.5) and optical grease (0.1mm thickness, reflectivity 1.41) were placed between the bottom of the crystal and the Silicon photomultiplier (SiPM) array. The SiPM utilized in the model was the Micro-30035-TSV model manufactured by ONSEMI, featuring a 16×16 array with a sensitive area of $3.07mm \times 3.07mm$ and a package area of $3.16mm \times 3.16mm$[25].

The physical property parameters of lanthanum bromide crystals mainly include the crystal's emission spectrum, light yield, decay time constant, refractive index, and intrinsic resolution. The emission spectrum of LaBr$_3$(Ce) crystals varies with the content of Ce. As the concentration of Ce increases, the light yield changes slightly, but the decay time is shortened. Generally, the decay time constant includes a fast time constant and a slow time constant. Since the fast decay component of the decay time constant of LaBr$_3$: 5% Ce crystal reaches 97%, the decay time constant is set to include only the fast component. The fast time constant is set to 15 ns, and the yield value is set to 1 [26,27]. The light yield (scintillation yield, SCY) of the crystal is set to 63000/MeV, and the refractive index of the crystal is set to 1.85[27]. In GEANT4, the emission spectrum obtained from physical experiments [28] is used to establish the emission spectrum of the crystal model. The largest characteristic of lanthanum bromide crystals lies in the presence of radioactive materials [138]La and [227]Ac within the crystals. The existence of these two radioactive nuclides endows lanthanum bromide crystals with inherent radioactivity, and their background energy spectrum is slightly different from the natural background spectrum. In the low-energy part (0-1800 keV), the background spectrum is mainly due to gamma transitions of [138]La (789 keV-1436 keV). When simulating the background spectrum, we calculate the total activity of [138]La based on the volume of the detector crystal and randomly disperse it inside the crystal (the volume activity of [138]La is 1.52 Bq/cm^3) [29,30], with a total activity of 19.7 Bq. Due to the small size of the crystal, it has a lower absorption capacity for gamma rays at 789 keV and 1436 keV, which has a minimal impact on the imaging results. In the high-energy part (1800 keV-2800 keV), the rays mainly come from [227]Ac and high-energy rays in the environmental background. Since the total count of high-energy rays is small, their impact on energy spectrum measurement and imaging results is minimal.

In the simulation study, the process of transporting optical photon can be divided into two main parts. The first part involves the transportation of optical photon within the medium, and the user can select the material parameters. These material parameters primarily include the emission spectra, scintillation yield, intrinsic resolution, and fast component of the scintillator. They play a crucial role in determining the production of optical photon and their transport through the medium. The second part involves the transportation of optical photon between different media,

requiring the user to specify the surface parameters. The primary surface parameters include type, finish, efficiency, reflectivity, and reflectivity type. These parameters control the physical interaction of optical photon at the surface between different media. The simulation program primarily utilizes the modular physics process FTFP_BERT, which involves replacing the electromagnetic interaction process with the standard electromagnetic process G4EmStandardPhysics_option1. Additionally, the program incorporates the optical process G4OptialPhysics.G4EmStandardPhysics_option1 encompasses various fundamental electromagnetic interactions, such as the photoelectric effect, Compton scattering, pair production, Coulomb scattering, and bremsstrahlung. On the other hand, the optical processes implemented in the program include scintillation, Cherenkov radiation, Rayleigh scattering, Mie scattering, refraction, and reflection.

(a)Scanning path

(b)The response energy spectrum by irradiation at different block
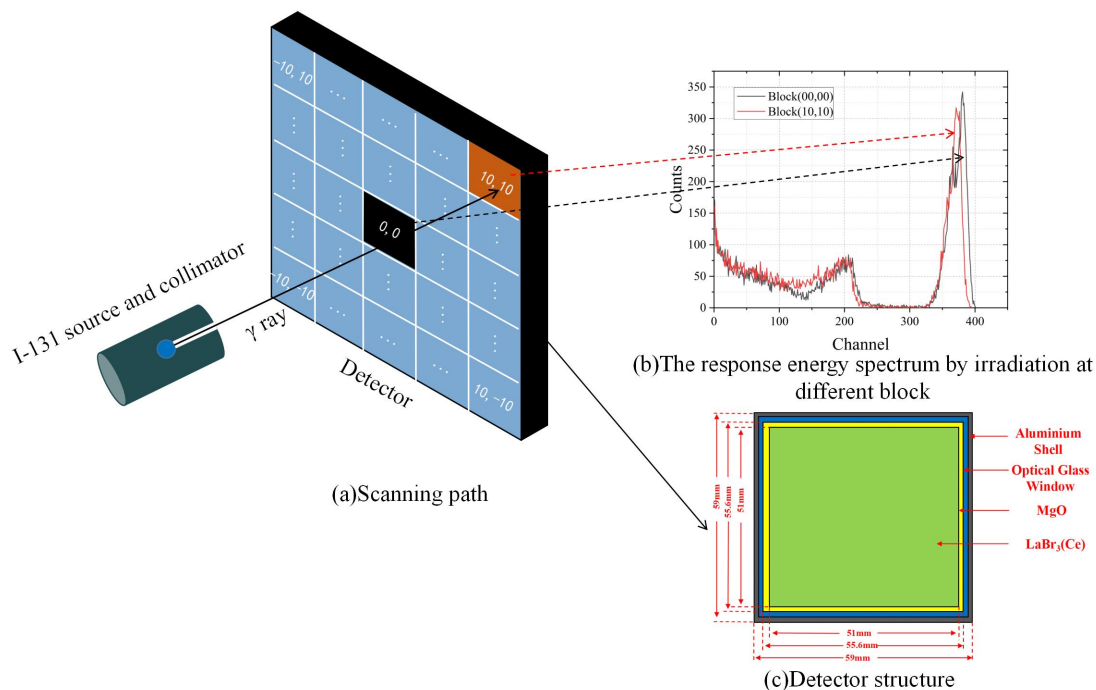
(c)Detector structure

Figure 1. Schematic diagram of imaging detector simulation experiment

The effective detection area of the imaging detector composed of monolithic crystals is artificially divided into 441 blocks. Located 180 mm in front of the imaging detector, the emission position and direction of gamma rays are set using the Class PrimaryGeneratorAction to simulate a point source. The I-131 radioactive source is placed within a tungsten shielding canister, located on the incident side of the imaging detector. The tungsten shielding canister is equipped with a collimation hole, allowing the γ-rays emitted by I-131 to be perpendicularly incident on the detector. By employing a step-scanning method, each block is scanned to obtain the detector response corresponding to all positions where the rays enter the crystal. When gamma rays enter the detector from a certain block and interact with the scintillator to produce photons, these photons are converted into electrical signals by the SiPM array. The signals from 256 SiPMs are summed to serve as the detector's energy response. Subsequently, the summed signal of the SiPM array is statistically

processed to obtain the gamma ray spectrum for each incident block. Then, the peak channel of the gamma ray spectra for each incident region are extracted. Due to the event occurring near the center of the crystal, the detected fluorescence distribution is relatively complete. The fluorescence distribution would be truncated. Therefore, we use the peak position of the central block (00,00) as the standard peak position, and establish a linear relationship matrix with the peak position of the gamma spectrum of each block. Thus, the peak channel of the spectrum in Block (00,00) is used as the standard peak channel. A linear relationship matrix is established between the peak channel of the gamma ray spectra corresponding to each block and that of Block (00,00). Finally, using the peak channel of Block (00,00) as the standard, the spectra of the other blocks are corrected so that the peak channel of all blocks align with that of Block (00,00). This results in the corrected spectral response of the detector.

In the simulation experiment, we obtained the gamma ray energy spectra at various detector blocks for ten common energies. Ten distinct spectral peaks are clearly visible in the spectra, confirming the feasibility of the established model [24]. We isolated the characteristic peak at 365 keV, resulting in Figure 1b. Notably, within the detector, there is a significant the spectral drift related to incident position from Block (00,00) to Block (10,10), which intensifies with increasing energy, making the phenomenon more pronounced. Given the limited variety of radiation sources in the laboratory, to more rigorously compare simulation results with experimental results, the spectral channel corresponding to the 365 keV peak were isolated from the simulation dataset. This extraction provided the 365 keV peak channel across various block for subsequent analysis, as shown in Figure 2a. The correlation between the 365 keV peak channel and their spatial positions indicates that the displacement is minimal at the center and increases towards the periphery, suggesting a positive correlation between displacement magnitude and proximity to the central axis—the peak displacement is minimal at the center and gradually increases towards the periphery. This phenomenon is caused by the interaction of gamma rays with the crystal lattice, leading to ionization and excitation of lattice atoms, followed by photon emission during de-excitation. The interaction of photons with the crystal includes processes of absorption, refraction, and reflection, with backscattering playing a more significant role in the peripheral areas. Additionally, photons traversing the crystal are modulated by the crystal structure and physical properties, affecting their trajectories and leading to photon flux attenuation. In turn, this results in spatial heterogeneity of the detector's intrinsic response characteristics, leading to position dependent energy responses to gamma ray.

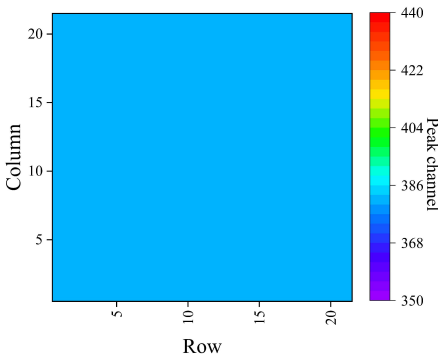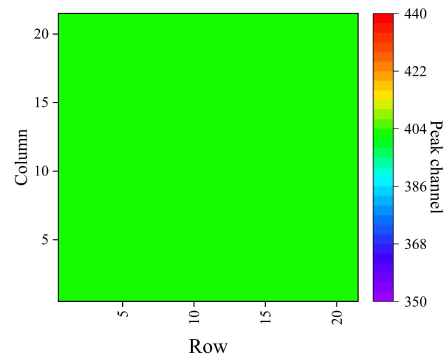Simulation experiment results　　　　　Physics experiment results
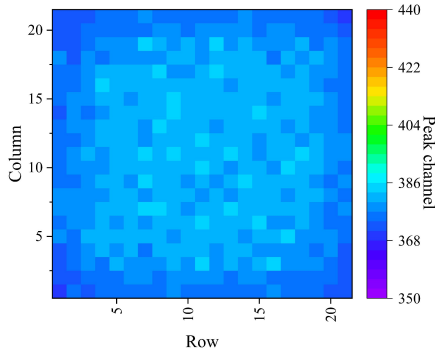
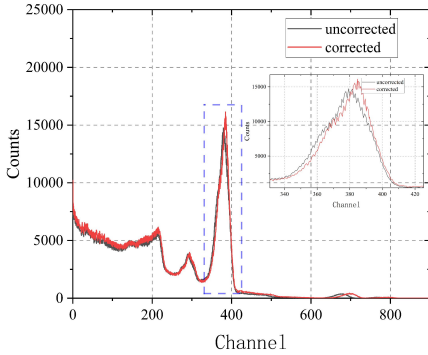(a) The uncorrected distribution map of the I-131 peak (@365keV)
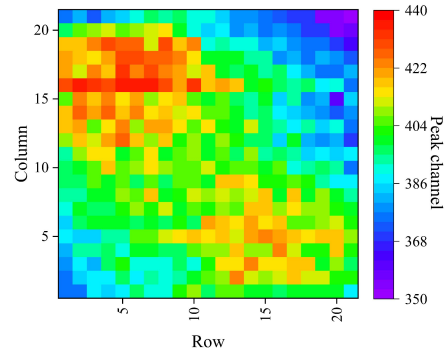
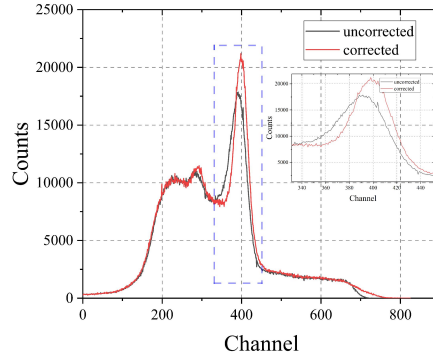(b) The uncorrected distribution map of I-131 peak (@365keV)

(c) The corrected distribution map of the I-131 peak (@365keV)

(d) The corrected distribution map of the I-131 peak (@365keV)

(e) Uncorrected and corrected I-131 energy spectra

(f) Uncorrected and corrected I-131 energy spectra

Figure 2. Uncorrected and corrected experiment results in simulation and physics experiment

2.2 Physical experiment

Figure 3 shows the radiation imaging system. The radiation imaging system primarily consists of one encoding plate (MURA-11), one imaging detector, one electronic system, one Jetson Xavier NX, and one display unit. The imaging detector

primarily consists of a LaBr$_3$(Ce) crystal coupled to an SiPM array. This paper utilizes the SiPM array model ARRAYJ−30035−64P manufactured by Onsemi. By assembling four of these arrays, a 16×16 detector array is formed, yielding a total of 256 channels of output signals. The ARRAYJ−30035−64P consists of $3mm \times 3mm$ J-series sipm arranged in an 8×8 array. Four SiPM arrays are fixed to the front of the interface board through connectors on the back, leaving a 1mm gap between each SiPM array to facilitate the packaging of the detector. The back of the interface board is composed of 4 pairs of connectors for the bias voltage input and initial signal readout of the SiPM arrays. All sensor substrates (cathodes) are combined to form a common I/O. After the internal packaging of the detector is completed, it is fixed to the detector housing through the mounting holes at the four corners of the interface board. In the design of the interface board, due to the lack of extensive copper plating on the board and light leakage from the connector itself, black tape is used for further light shielding treatment of the detector to achieve a better light shielding effect. The electronic system comprises Symmetric Charge Division Circuit (SCDC), Amplitude Time Convert Circuit (ATCC) and Digital Signal Processing Circuit (DSPC). ATCC initially employs the AD8066 operational amplifier to perform signal summation and amplification, scaling the signal to a suitable amplitude for input into a hysteresis comparator circuit. The comparator utilizes the TLV350 device, and the hysteresis comparison circuit shapes the nuclear pulse signal into a rectangular pulse signal. The 256-channel signals read out from the SiPM array detector is divided into 32-channel signals through the summing circuit and is inputted into DSPC via an FPC interface for FPGA acquisition. DSPC incorporates a Xilinx 7 Series core board along with a system power board. The core board, through its 32 I/O ports, captures the 32-channel rectangular pulse signals outputted by the conditioning board. A single channel signal that has undergone A/D conversion is acquired by the FPGA for filtering shaping, peak value extraction, and energy spectrum analysis. The 33-channel signal data (32-channel rectangular pulse signals and 1-channel ADC data) processed by the core board are transmitted to the Jetson Xavier NX for further processing via Ethernet. The Jetson Xavier NX is NVIDIA's edge computing platform, utilized for the deployment of 32-FCNN localization algorithms and maximum likelihood estimation algorithms（MLEM）, enabling parallel computation of these algorithms to achieve the goal of algorithm acceleration. Ultimately, the reconstructed images and other information about the radioactive sources are displayed on the monitor. In a physical experiment analogous to simulation experiments, an ^{131}I source is positioned at a distance of 180 mm from the detector. A step-scanning method is utilized, where radiation is incident perpendicularly onto the detector surface through a collimator. The detector captures the energy response at different incident positions. In the step-scanning process, a collimator with a hole diameter of 2.5mm, an overall diameter of 33mm, and a thickness of 55mm is used to collimate the gamma rays emitted by ^{131}I. Subsequently, the effective detection area of the detector is gridded, also in the manner of the simulation experiment, by uniformly dividing the effective detection area of the detector into 441 blocks. The ^{131}I source (the activity is 0.1mCi) is placed above the

collimator, marking the incident position as (x, y). Each point is measured for 4 minutes, and the summed signal V_{xy} from the SiPM array at position (x, y) is acquired through the multi-channel signal acquisition board. Finally, the energy spectrum E_{xy} at the incident position is statistically derived from signal V_{xy} using the upper computer, completing the process of a single step scan. Step scanning involved a total of 441 measurement points, with a total duration of 29.4 hours.

Figure 2b illustrates the distribution of the 365 keV characteristic peaks for Block (00,00) and Block (10,10) in a physical experiment. The experimental data closely align with the results obtained from Monte Carlo (MC) simulations. The variation in pulse height channel addresses is notably pronounced due to the different incident positions of the radiation. During the interaction of gamma rays with the crystal, ionization and excitation of the crystal atoms occur, and the de-excitation process emits photons. These photons may be absorbed, refracted, and reflected by the crystal, with edge positions being more significantly affected by backscattering. Moreover, the propagation of photons within the crystal is influenced by its structure and physical properties, altering their direction and causing light loss. This results in inconsistent energy responses of monolithic crystal detectors The overall peak position indicates that the closer to the center position, the smaller the spectral drift related to incident position, and the closer to the peripheral position, the more severe the spectral drift related to incident position, which is similar to the simulation results. Additionally, in electronic hardware, due to manufacturing variations, SiPM manufacturers cannot ensure that each SiPM has identical properties. The response of the SiPM array, as well as the acquisition and readout of signals, cannot be perfectly synchronized, further exacerbating the inconsistency of peak positions and increasing the severity of the spectral drift related to incident position, with a maximum difference of 84 channels. Although SiPMs exhibit a certain degree of temperature drift, the entire experimental process was conducted at room temperature, with the signal processing circuit board and FPGA chip essentially maintaining a constant temperature. Therefore, spectral drift caused by temperature can be considered negligible.
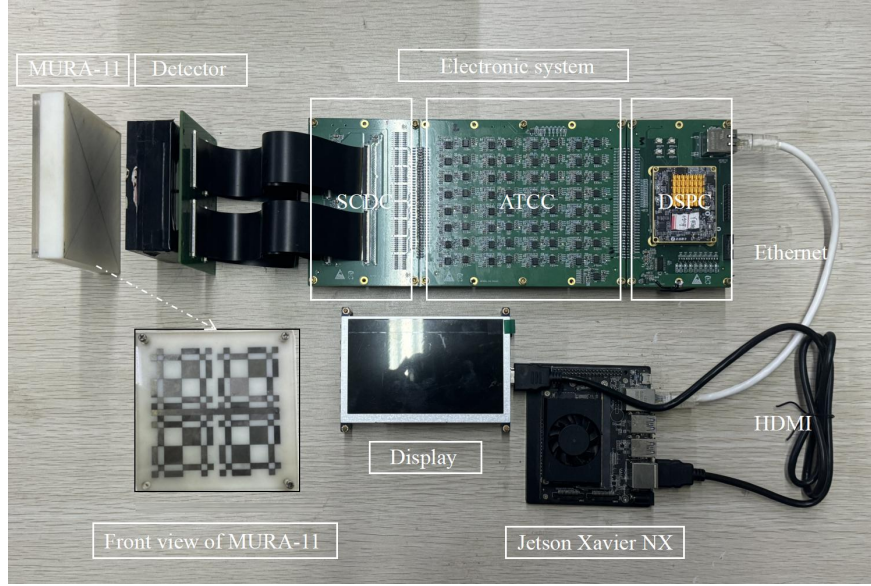
Figure 3. Radiation imaging system

3. Correction method and results

In light of the characteristics of this class of detectors, the method and principle for energy response functional correction matrix have been proposed. We evaluated and discussed the correction effects on peak consistency from four aspects: full-energy peak consistency, energy resolution, encoded images, and reconstruction image quality.

3.1 Correction method

In preliminary simulation studies, we extracted the peak channels of each full-energy peak in the energy range of 300keV to 2000keV for various blocks. Since there is a linear relationship between the channel of the peak and the energy of peak, there should also be a linear relationship between each characteristic peak in each block [24]. Therefore, in physical experiments, we can also use a functional correction matrix to improve full-energy peak consistency. However, the functional correction matrix needs to be recalibrated. Thus, we investigated the linear relationship between the full-energy peak of the central Block (00,00) and other blocks through physical experiments. Since step-scanning experiments have certain requirements for the type, activity, and size of the radiation source, the laboratory can only provide I-131 that meets the requirements. Secondly, because the calibration of the functional correction matrix requires full-energy peaks of two or more energies, we selected the two characteristic peaks of I-131 at 284keV (branching ratio of 6.12%) and 365keV (branching ratio of 81.5%) for matrix calibration. Figure 4a demonstrates the linear relationship between the 284keV and 365keV characteristic peaks of the central Block (00,00) and the peripheral Block (09,08), Block (10,10) in physical experiments. Among them, the linear relationship formula between Block (00,00) and Block (10,10)

is $y_{(10,10)} = 0.98x - 36.29$, $k_{(10,10)} = 0.98$, $b_{(10,10)} = -36.29$. The linear

relationship formula between Block (00,00) and Block (09,08) is $y_{(09,08)} = 1.02x -$

38.71 , $k_{(09,08)}$ =1. 02, $b_{(09,08)}$ =− 38.71 . Thus, the function correction matrix is

composed of the coefficients (k, b) from the linear equation. Establish a linear parameter fitting line between the spectral channel address of the Block (i, j) and the spectral channel address of the Block (00, 00) detector, with the linear relationship

$y_{(i,j)} = k_{(i,j)}x + b_{(i,j)}$. Here, $y_{(i,j)}$ represents the channel address of the peak for

Block (i, j), x indicates the channel of the peak for the central Block (00,00), $k_{(i,j)}$

denotes the slope for Block (i, j), and $b_{(i,j)}$ represents the y-intercept for the Block (i,

j). Ultimately, a function correction matrix $(k_{(i,j)}, b_{(i,j)})$ is obtained, as shown in

Equation (1).

$$\left\{ \begin{array}{c} \left(k_{(-10,10)}, b_{(-10,10)}\right) \cdots\cdots \left(k_{(10,10)}, b_{(10,10)}\right) \\ \left(k_{(-10,09)}, b_{(-10,09)}\right) \cdots\cdots \left(k_{(10,09)}, b_{(10,09)}\right) \\ \vdots \quad \left(k_{(00,00)}, b_{(00,00)}\right) \quad \vdots \\ \left(k_{(-10,-09)}, b_{(-10,-09)}\right) \cdots\cdots \left(k_{(10,-09)}, b_{(10,-09)}\right) \\ \left(k_{(-10,-10)}, b_{(-10,-10)}\right) \cdots\cdots \left(k_{(10,-10)}, b_{(10,-10)}\right) \end{array} \right\} \quad (1)$$

Based on the functional relationship between the incident position and energy discovered in this study, the energy response functional correction matrix is proposed to correct the energy response and improve the consistency of full-energy peaks. Firstly, a step-scanning method was employed to calibrate the correction matrix of the detector. This means that gamma rays were incident perpendicularly onto the detector through a collimator, and the response signals from the SiPM array of the detector were summed and statistically analyzed for energy spectra, from which the full-energy peaks and coordinate information were extracted. By using a linear function, the coefficients for the peak channel of each block relative to the central block's peak channel were obtained, thus acquiring the detector's complete energy response functional correction matrix. Ultimately, by using the coordinate information of the interaction between the rays and the detector. And based on the principle of "look-up table" method, the correction coefficients corresponding to the coordinates in the energy response functional correction matrix were found. Thereby correcting the peak channel of each interaction event at different locations, and subsequently correcting the entire detector's energy response, as shown in Figure 4b. In Figure 4b, $E_{(i, j)}$ is the uncorrected peak address, (k, b) constitutes the functional correction matrix, and $E'_{(i, j)}$ is the corrected peak address.

This imaging system utilizes a ray localization algorithm based on neural network to obtain positional information of the rays [23]. The principle is that when rays interact with the detector, the SiPM at the interaction point receives the strongest pulse signal intensity, and as the scintillation light propagates within the crystal, the signal strength of the SiPM at other locations gradually decreases. Therefore, the position of the rays

can be located based on the distribution of light intensity across the SiPM array. In this imaging system, the 256-channel SiPM signals are summed and converted into 32-channel signals, which are used as input data for a fully connected neural network to perform neural network ray localization, thus obtaining positional information.
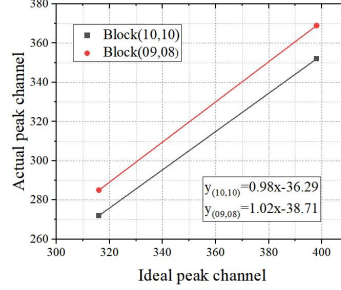
(a)Relationship between peak positions at different locations and the central position
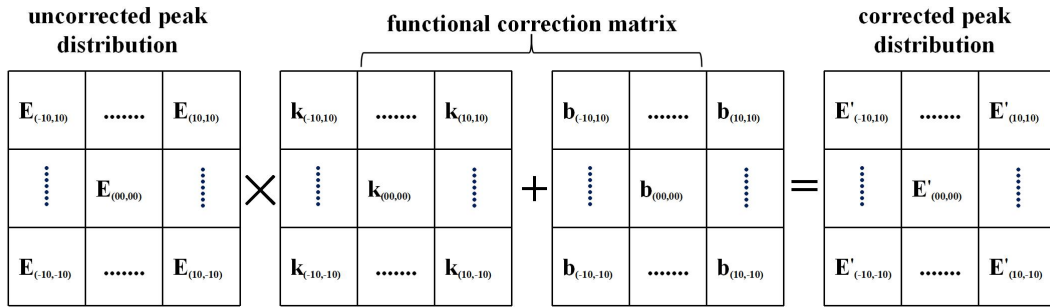
(b)Correction method

Figure4. Energy response correction process

3.2 Correction results

To better compare the uncorrected and corrected results from both simulation and physical experiments, the measurement object in this study for both simulation and physical experiments is the characteristic gamma rays emitted by I-131. The correction results will be discussed in terms of consistency of uncorrected and corrected peak positions, energy resolution, encoded images, and reconstruction image quality.

From the consistency of full-energy peaks, the energy response functional correction matrix was obtained separately from simulation and physical calibration experiments, and the energy response for both simulated and physical experiments were corrected, resulting in a significant improvement in full-energy peaks consistency. Figure 2c illustrates the corrected 365keV peak for various incident block in the simulated experiment, while Figure 2d shows the same for the physical experiment. It can be observed from the figures the peaks in the edge blocks have been significantly corrected in simulation and physical experiments. And the consistency of full-energy peak has been markedly enhanced, essentially converging to uniformity. Additionally, within the energy range of 365-1332keV, the results of the simulation experiment are well-fitted to the energy response functional correction

matrix [24]. The energy response functional correction matrix is designed to channel the 284 keV and 365 keV energies of I-131 in the physical experiment. Consequently, the peak channel error is corrected to zero channels in the physical experiment.

Due to inconsistent responses to uncorrected peaks, there is a variation in the energy resolution of the detector. When incident gamma rays are predominantly absorbed by the edge blocks of the detector, the energy resolution of the detector is decreased. Conversely, when the central block of the detector primarily absorbs the incoming rays, the energy resolution is improved. Thus, enhancing the consistency of the detector's full-energy peak can also improve the energy resolution to a certain extent. The energy response functional correction matrix is obtained separately from simulation and physical calibration experiments to correct energy response in both simulated and physical experiments, resulting in an improvement in energy resolution. The energy resolution at the 365keV energy uncorrected and corrected in the simulation and physical experiments is shown in Figure 2, where Figure 2e compares the energy resolution at the 365keV energy uncorrected and corrected in the simulation experiment, and Figure 2f does the same for the physical experiment. By comparison, the full-width at the half of the maximum (FWHM) of the corrected gamma-ray spectrum is narrowed, the peak count is obviously increased, and the energy resolution is improved. In the simulation experiment, the FWHM of the characteristic peak at 365keV was reduced from 38 channels to 32 channels, increasing the energy resolution by 18.8%. In the physical experiment, the FWHM of the characteristic peak at 365keV was reduced from 53 channels to 38 channels, increasing the energy resolution by 28.3%. The improvement of the energy resolution of the imaging detector plays a key role in the selection of the energy window data and the improvement of the quality of the reconstructed image.

In the imaging applications of coded aperture gamma imaging systems, data is selected based on the energy window. Due to the inconsistent response to uncorrected peaks, the detection efficiency and the loss of real events will be reduced, which will affect the image quality. In more severe cases, it can lead to incomplete projected images and ultimately failing to form an image, especially when the incident rays are mainly absorbed by the edge block of the detector. Therefore, it is necessary to correct the full-energy peak consistency in the effective detection area of the detector to improve the imaging quality. In the study of this paper, both the simulation and physical experiments utilized a radioactive source of ^{131}I $(T_{\frac{1}{2}} = 8.02d)$ with an activity of 0.1mCi. The center of the ^{131}I point source, the encoding board collimator, and the imaging detector are aligned horizontally on the same axis. The distance between the ^{131}I point source and the detector is 80 cm, and the distance between the encoding board collimator and the detector is 5 cm. The MURA array can be represented by a matrix B_{ij}, where r denotes the number of rows (or columns) in the matrix, which is a prime number. $B_{ij} = 1$ indicates an open aperture, and $B_{ij} = 0$ indicates a closed aperture [31].

$$B_{ij} = \begin{cases} 0, & if\ i = 0 \\ 1, & if\ j = 0, i \neq 0 \\ 1, & if\ C_r(i)C_r(j) = 1 \\ 0, & otherwise \end{cases} \tag{2}$$

In which，$0 \leq i \leq r - 1$；

$$C_r(i) = \begin{cases} 1, \left(1 \leq x \leq r, if\ i = mod_r^{x^2}\right) \\ -1, \qquad\qquad otherwise \end{cases} \tag{3}$$

The structure of the nested MURA coded aperture is derived from the MURA $(N \times N)$ by expanding the MURA coded aperture in a centrally symmetric manner to nine times its original size, resulting in the Loop MURA $(3N \times 3N)$. Subsequently, a coded aperture of size $(2N - 1) \times (2N - 1)$ at the central position is selected to serve as the Nested MURA [31]. After the interaction of radiation with the crystal, a neural network localization algorithm is employed to acquire the encoded image on the detector. Figures 5a and 5b represent the uncorrected and corrected encoded images from the physical experiment respectively. In Figure 5a, which is the uncorrected encoded image, data loss is observed in the upper right and lower left corners, with more significant loss in the lower right corner. This is attributed to the loss of true events in the upper right and lower left blocks as shown in Figure 2b, leading to imprecise energy window data. The uncorrected encoded images in the physical experiment are severely hampered by data loss, rendering image reconstruction infeasible. In addition to the event positions causing peak inconsistencies, the manufacturing process of SiPMs by manufacturers cannot guarantee identical performance for each SiPM. The response of the SiPM array, signal acquisition and readout are not perfectly synchronized, which further aggravate the inconsistency of full-energy peaks and reduces the amount of effective encoded images data. The corrected encoded images are more complete, enabling a clearer reconstruction of the images.

When the radioactive source is located at the center of the imaging detector's useful field of view (UFOV), most of the valid information is collected in the central area of the detector. An incomplete encoded image will not lead to a failure in image reconstruction, and it is also possible to accurately reconstruct the position of the radioactive source. In this case, inconsistencies in full-energy peaks can introduce artifacts in the reconstructed image, reducing the signal-to-noise ratio (SNR) and affecting the quality of the reconstructed image. However, when the radioactive source is located at the edge of the imaging detector's UFOV, most of the valid information is concentrated in the peripheral area of the detector. The existence of inconsistent full-energy peaks can cause severe loss of valid information, leading to deviations in the position of the radioactive source in the reconstructed image, or even failure to image. Figures 5c and 5d represent the uncorrected and corrected reconstructed images from the physical experiment, respectively. The SNR of the uncorrected reconstructed image is only 2.38. The corrected peak channel eliminates the data that does not belong to the energy window and improves the detection efficiency of the detector. At the same time, it also improves the energy resolution of the imaging detector, and the SNR is significantly enhanced, from 2.38 to 5.37, an

increase of 125.6%. It can be seen from Figure 5 that the energy resolution of the uncorrected imaging detector is poor, resulting in the data not belonging to the energy window being recognized as valid data. This results in a low SNR and the presence of artifacts in the reconstructed image. The SNR of the corrected reconstructed image is improved, reducing or eliminating artifacts, and enhancing the quality of the reconstructed image.
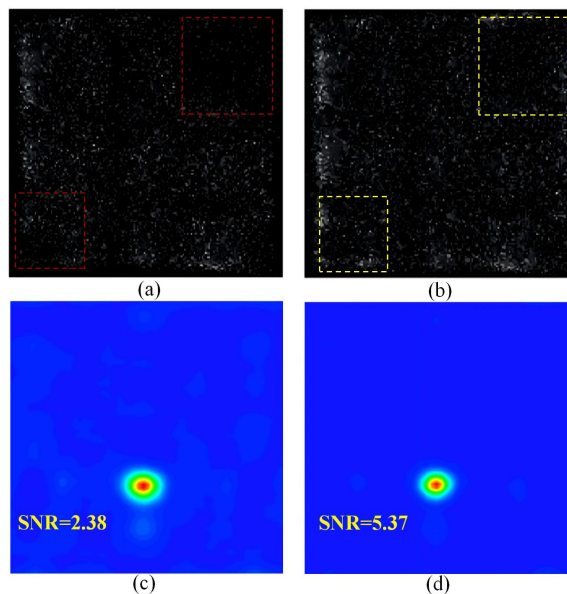

Figure 5. Imaging physics experiment

4. Conclusion

This study has found that in addition to the full-energy peaks inconsistencies in array-type crystals, monolithic crystal detectors also exhibit the same phenomenon. The different incident positions of gamma rays will also cause the change of the energy deposition of the monolithic crystal detector, which will lead to the inconsistency of the full-energy peaks. This leads to a decrease in energy resolution, deterioration of energy linearity, and a reduction in isotope identification capability. For measurement systems with fixed ROI, it results in a decrease in the number of particles within the ROI, reducing detection efficiency and thereby affecting measurement accuracy and increasing measurement errors. By performing step-scanning to obtain the full-energy peaks at different incidence positions, and based on the linear relationship between the peak channel of each block and the central block, the energy response functional correction matrix for the detector is obtained. A neural network localization algorithm is used to position the incident rays and obtain positional information. According to this positional information, the corresponding correction coefficients from the energy response functional correction matrix are matched, thereby correcting the detector's energy response. In simulation experiments, this method improves the consistency of the full-energy peaks, and decreases the FWHM of the 365 keV characteristic peak from 33 channels to 28 channels, improving energy resolution by 15.2% and enhancing detection efficiency.

In physical experiments, this method improves the consistency of the full-energy peaks of the monolithic crystal imaging detector and makes the peaks of the detector plane evenly distributed. In terms of energy resolution, the method reduces FWHM from 53 channels to 38 channels at the characteristic peak of 365keV, and the energy resolution is increased by 28.3%. In the aspect of image reconstruction, the method reduces the artifacts in the reconstructed image, improves SNR from 2.38 to 5.37, and even converts the incomplete encoded image into the fully encoded image to achieve more accurate image reconstruction. The method proposed in this study minimizes or eliminates the impact of energy response inconsistencies, enhances the detector's energy resolution, allows for more accurate energy window selection in imaging detectors, and improves image quality. It is of great significance to improve the accuracy of nuclide identification and enhance the quality of energy spectrum imaging.

Reference:

[1] S. Sun, Y. Liu, X. Ouyang et al., Near-field high-resolution coded aperture gamma-ray imaging with separable masks. Nucl Instrum Meth A. 951, 163001 (2020). https://doi.org/10.1016/j.nima.2019.163001

[2] R. Pani, R. Pellegrini, P. Bennati et al., Investigation on a small FoV γ camera based on LaBr3:Ce   continuous crystal. Nucl Phys B-Proc Sup. 197, 202–205 (2009). https://doi.org/10.1016/j.nuclphysbps.2009.10.067

[3] R. Wojcik, S. Majewski, High spatial resolution γ imaging detector based on a 5'' diameter R3292 Hamamatsu PSPMT. IEEE T Nucl Sci. 45, 487–491 (1998). https://doi.org/10.1109/23.682432

[4] X.L. Shen, P. Gong, X. B. Tang et al., Encoding methods matching the 16×16 pixel CZT detector of a coded aperture gamma camera. Nucl Sci Tech. 31, 92 (2020). https://doi.org/10.1007/s41365-020-00796-5

[5] H.J. Kim, H. Back, K. S. Joo., Development of a wireless radiation detection backpack using array silicon-photomultiplier (SiPM). Nucl Eng Technol. 52(2):456-460 (2020). https://doi.org/10.1016/j.net.2019.07.027

[6] D. Renker., Geiger-mode avalanche photodiodes, history, properties and problems. Nucl Instrum Meth A. 567(1):48-56 (2006). https://doi.org/10.1016/j.nima.2006.05.060

[7] S. Ghosh, S. Mallick, K. Banerjee, et al., Low-noise mid-wavelength infrared avalanche photodiodes. J Eelctron Mater. 37(12):1764-1769 (2008). https://link.springer.com/article/10.1007/s11664-008-0542-0

[8] N. Otte, B. Dolgoshein, J. Hose, et al., The SiPM—A new photon detector for PET. Nucl Phys B-Proc Sup, 150:417-420 (2006). https://doi.org/10.1016/j.nuclphysbps.2004.08.048

[9] R. Agishev, A. Comerón, J. Bach, et al., Lidar with SiPM: Some capabilities and limitations in real environment. Opt Laser Technol. 49:86-90 (2013). https://doi.org/10.1016/j.optlastec.2012.12.024

[10] M. Grodzicka, M. Moszyński, T. Szczęśniak, et al., Energy resolution of small scintillation detectors with SiPM light readout. J Instrum. 8(02): 2017 (2013). https://iopscience.iop.org/article/10.1088/1748-0221/8/02/P02017

[11] Z. Lin, B. Hautefeuille, S. Jung, et al., The design of a scintillation system based on SiPMs integrated with gain correction functionality. Nucl Eng Technol. 52(1):164-169 (2020). https://doi.org/10.1016/j.net.2019.07.005

[12] H. Miyamoto, I. Minoura, K. Okamoto, et al., SiPM interdisciplinary application in the fields of astroparticle physics and bio-molecular science. Nucl Instrum Meth A. 695:87-90 (2012). https://doi.org/10.1016/j.nima.2011.11.078

[13] R. G. Shi, Y. Chen, M. F. Wei., Least squares estimate algorithm based on particle swarm optimization for position reconstruction of scintillation crystal. J Instrum. 13(12):12029-12029 (2018). https://beta.iopscience.iop.org/article/10.1088/1748-0221/13/12/P12029

[14] A. Fabbri, D. Sacco, P. Bennati, et al., Study of position reconstruction of a LaBr3: Ce continuous，scintillation crystal for medical applications. J Instrum. 8(12):12010-12010 (2013). https://iopscience.iop.org/article/10.1088/1748-0221/8/12/P12010/meta

[15] W. Siman, S. C. Kappadath, Performance characteristics of a new pixelated portable gamma camera. Med Phys. 39(6):3435-3444 (2012). https://aapm.onlinelibrary.wiley.com/doi/10.1118/1.4718874

[16] Y. Li, C. Wang, L. Y. Liu, et al., Development and performance calibration of position sensitive detector based on LaBr3(Ce) crystal coupled with SiPM. Nucl Tech. 45(07):53-58 (2022). (in Chinese) https://doi.org/10.11889/j.0253-3219.2022.hjs.45.070401

[17] Y. Li, Q. Wang, X. C. Huang, et al., Detector design and performance test for coded camera of large area and high sensitivity. Nucl Tech. 43(05):33-38 (2020). (in Chinese) https://doi.org/10.11889/j.0253-3219.2020.hjs.43.050402

[18] V. O. Cencelli, F. D. Notaristefani, A. Fabbri, et al., A gamma camera with the useful field of view coincident with the crystal area. IEEE Nucl Sco Conf R. 1886-1890 (2009). https://ieeexplore.ieee.org/document/5402162

[19] A. Fabbri, P. Bennati, V.O. Cencelli, et al., A new iterative algorithm for pixilated and continuous scintillating crystal. Nucl Instrum Meth A. 648:79-84 (2011). https://doi.org/10.1016/j.nima.2010.12.136

[20] R. G. Shi, Y. Chen, X. J. Dang, et al., Experimental evaluation of reconstruction algorithms for scintillation crystal array based on charge projection readout. Nucl Instrum Meth A. 937:117-124 (2019). https://doi.org/10.1016/j.nima.2019.05.064

[21] W. Lee, G. Cho, S. W. Lee, et al., Simulation of maximum-likelihood position estimation in small gamma camera with position-sensitive photomultiplier tube (PSPMT). IEEE Nucl Sci Conf R. 4:1915-1918 (2001). https://ieeexplore.ieee.org/document/1009198

[22] P. Bruyndonckx, S. Léonard, S. Tavernier, et al., Neural network-based position estimators for PET detectors using monolithic LSO blocks. IEEE T Nucl Sci. 51(5):2520-2525 (2004). https://ieeexplore.org/document/1344371

[23] W. Lu, H. W. Zhang, M. Z. Liu, et al., Generalization ability of a CNN γ-ray localization model for radiation maging. Nucl Sci Tech. 34, 185 (2023). https://doi.org/10.1007/s41365-023-01323-y

[24] H. X. Li, L. Wang, W. Lu, et al., A study on "position-energy" response correction method based on monolithic crystal coupled SiPM array. Nukleonika. 69(3):169-176 (2024). https://sciendo.com/article/10.2478/nuka-2024-0024

[25] W. Lu, L. Wang, Y. Yuan, et al., Monte Carlo simulation for performance evaluation of detector model with a monolithic LaBr_3(Ce) crystal and SiPM array for γ radiation imaging. Nucl Sci Tech. 33(08):165-176 2022. https://doi.org/10.1007/s41365-022-01081-3

[26] E.V.D. van Loef, P. Dorenbos, C.W.E. van Eijk, et al., Scintillation properties of LaBr3:Ce3+ crystals: fast, efficient and highenergy-resolution scintillators. Nucl Instrum Meth A. 486, 254–258 (2002). https://doi.org/10.1016/S0168-9002(02)00712-X

[27] J. Glodo, W.W. Moses, W.M. Higgins et al., Effects of Ce concentration on scintillation properties of LaBr 3:Ce. IEEE Nucl Sci Conf R. 52, 1805–1808 (2005). https://doi.org/10.1109/NSSMIC.2004.1462374

[28] S. Raffaele, P. Roberto, P. Rosanna et al., MgO reflectance data for Monte Carlo simulation of LaBr3Ce scintillation crystals. Nucl Instrum Meth A. 701, 44–53 (2013). https://doi.org/10.1016/j.nima.2012.10.060

[29] H. Cheng, B. H. Sun, L. H. Zhu, et al., Intrinsic background radiation of LaBr3(Ce) detector via coincidence measurements and simulations. Nucl Sci Tech.31,33-34 (2020). https://doi.org/10.1007/s41365-020-00812-8

[30] C. L. Zhao, Y. P. Li, L. H. Chen, et al., Experimental Study of Lanthanum Bromide Detector in the Gamma ray Imaging. Appl Mech Mater. 336, 373-378 (2013). https://doi.org/10.4028/www.scientific.net/AMM.336-338.373

[31] S. R. Gottesman, E. E. Fenimore. New family of binary arrays for coded aperture imaging. Appl Optics. 28, 4344-4352 (1989). https://doi.org/10.1364/AO.28.004344